Physics Letters A 382 (2018) 3298–3305

Contents lists available at ScienceDirect

Physics Letters A

www.elsevier.com/locate/pla

Combined effect of the perpendicular magnetic field and dilute charged impurity on the electronic phase of bilayer AA-stacked hydrogenated graphene

Bui Dinh Hoi [a], Mohsen Yarmohammadi [b,*]

[a] Department of Physics, University of Education, Hue University, 34 Le Loi, Hue City, Viet Nam
[b] Lehrstuhl für Theoretische Physik I, Technische Universität Dortmund, Otto-Hahn Straße 4, 44221 Dortmund, Germany

ARTICLE INFO

Article history:
Received 23 August 2018
Received in revised form 18 September 2018
Accepted 20 September 2018
Available online 25 September 2018
Communicated by R. Wu

Keywords:
Bilayer hydrogenated graphene
Charged impurity
Magnetic field
Green's function
Born approximation

ABSTRACT

We address the electronic phase engineering in the impurity-infected functionalized bilayer graphene with hydrogen atoms (H-BLG) subjected to a uniform Zeeman magnetic field, employing the tight-binding model, the Green's function technique, and the Born approximation. In particular, the key point of the present work is focused on the electronic density of states (DOS) in the vicinity of the Fermi energy. By exploiting the perturbative picture, we figure out that how the interaction and/or competition between host electrons, guest electrons, and the magnetic field potential can lead to the phase transition in H-BLG. Furthermore, different configurations of hydrogenation, namely reduced table-like and reduced chair-like, are also considered when impurities are the same and/or different. A comprehensive information on the various configurations provides the semimetallic and gapless semiconducting behaviors for unfunctionalized bilayer graphene and H-BLGs, respectively. Further numerical calculations propose a semimetal-to-metal and gapless semiconductor-to-semimetal phase transition, respectively, when only turning on the magnetic field. Interestingly, the results indicate that the impurity doping alone affects the systems as well, leading to semimetal-to-metal and no phase transition in the pristine system and hydrogenated ones, respectively. However, the combined effect of charged impurity and magnetic field shows that the pristine bilayer graphene is not influenced much as the functionalized ones and phase back transitions appear. Tuning of the electronic phase of H-BLG by using both types of electronic and magnetic perturbations play a decisive role in optical responses.

1. Introduction

Graphene as a first two-dimensional (2D) carbon material is still a subject of extensive research in nanoscience in both scientific and engineering fields due to its remarkable electronic and physical properties such as the unconventional quantum Hall effect [1] and high carrier mobility [2–4]. However, the *pristine* graphene with inherent zero band gap is not applicable in logic circuits stemming from its fairly low on/off current ratio of about 4 [5]. To overcome this obstacle, one has to explore effective methods to open a band gap in its electronic spectrum, resulting in converting massless Dirac fermions to massive ones. In so doing, there are various approaches such as applying electric field [6,7], uniaxial strain [8,9], different substrates [10,11], cutting graphene [12,13], and chemical functionalization [14]. All of these ways break the electron–hole band symmetry and induce a finite (non-zero) band gap. To do the best way, one should be aware that the stability of the honeycomb lattice of graphene is conserved during the processes, i.e. during applying external perturbations. In addition on graphene, a new window in logic applications can be opened using the topological insulators with remarkable topological properties of edge states in dynamical superlattices [15]. Moreover, other applicable photonic Floquet topological insulators in honeycomb lattice of atomic ensembles give rise to fascinating features [16]. On the other hand, it is worthwhile to mention that for logic devices, the electro-optical properties of atomic systems alarm interesting outcomings [17,18].

Currently, hydrogenation of carbon materials has attracted considerable attention due to the widespread applications behind it. Hydrogenation of graphene induces different electronic and magnetic characterizations into the graphene, making it a proper candidate in logic devices with a non-zero band gap, which is estab-

* Corresponding author.
E-mail addresses: buidinhhoi@hueuni.edu.vn (B.D. Hoi), mohsen.yarmohammadi@tu-dortmund.de (M. Yarmohammadi).

https://doi.org/10.1016/j.physleta.2018.09.028
0375-9601/

lished both theoretically and experimentally in Refs. [19–26]. It has been shown that the full adsorption of hydrogen (H) atoms on top of carbon (C) atoms in graphene opens a band gap of 3.43 eV [27] and a net magnetic moment of 1 μ_B (μ_B being the Bohr magneton constant) [28,29]. Furthermore, ferromagnetic and antiferromagnetic ordering for different couplings between H and C atoms are reported [23]. One of the important factors leading to different properties in the hydrogenation of graphene refers to the hydrogenation configuration. It implies that fully hydrogenated graphene, which is called graphane has different responses compared to the half-hydrogenated one [20,30]. In addition to hydrogen, other chemical functionalizations with F, OH, COOH, and O give rise to fascinating properties in graphene [13, 30–32]. The main goal of functionalization of graphene is destroying sp^2-hybridization indeed. It should be noted that the hydrogenation process is reversible in order to tune the electronic phase of the system [19,33].

Unlike monolayer graphene, tuning of the band gap and electronic properties in bilayer graphene is easier originating from the *interlayer* coupling between C atoms from the top and bottom layers [34]. The same ways used in monolayer graphene in order to induce a band gap can be used in bilayer graphene too [5–7, 34–38]. The arrangement of electronic bands in bilayer graphene shows that the system is a semimetal [39,40]. Furthermore, the chemical modification of few-layer graphene by H atoms has been investigated well experimentally [41]. They found that the properties of hydrogenated-few-layer graphene depend strongly on the number of layers. On the one hand, it has been shown that the hydrogenated bilayer graphene is a ferromagnetic semiconductor [35], which of course, like the monolayer case, the hydrogen site-dependent physical properties are expected [19,21,22,26, 42–45]. On the other hand, stacking of layers is important. Bilayer graphene has different types of stacking including the Bernal (AB-stacked), the simple (AA-stacked), twisted, and so on [46–49]. In AB (AA) staking case, A/B atom in the first layer corresponds to B/A (A/B) atom in the second layer. Bilayer graphene and its hydrogenated version inherently have large potentials in real applications [5,35,50]. Generally, the hydrogenation of single-layer graphene is much easier than the bilayer case [19,33]. Although most of the references above are on AB-stacked bilayer graphene, to the best of our knowledge, a few investigations of hydrogenated AA-stacked bilayer graphene have been done to date.

Recently, there have been several studies on the magnetic field effect on bilayer graphene [51,52]. As well known, the thickness of 2D materials tells us that only the coupling between the magnetic field and spin degrees of freedom is possible, not the orbit one. It is better to say that the coupling from spins is more dominant than the orbit ones in 2D systems. For this reason, applying a magnetic field leads to various physical properties. Also, investigation of hydrogenated bilayer graphene subjected to a magnetic field beam is interesting. In addition, as mentioned before, optimizing electronic properties of bilayer graphene requires to control the band gap which has been done by numerous methods [see the previous paragraph]. Interestingly, impurity doping effects is also one of the ways to tune the physical quantities of low-dimensional materials [53–59]. This is also appealing in condensed matter physics to see what the impurity effects on the electronic phase of hydrogenated bilayer graphene are.

Motivated by the provided insights on hydrogenated bilayer graphene and different effective factors, we raise this question: What are the electronic treatments of the impurity-infected hydrogenated bilayer graphene (H-BLG) subjected to a uniform magnetic field with different H configurations? To answer this question, we restrict ourselves to the basic quantity, electronic density of states (DOS). Although, as mentioned, there are numerous works on bilayer graphene theoretically, a few reports can be found on

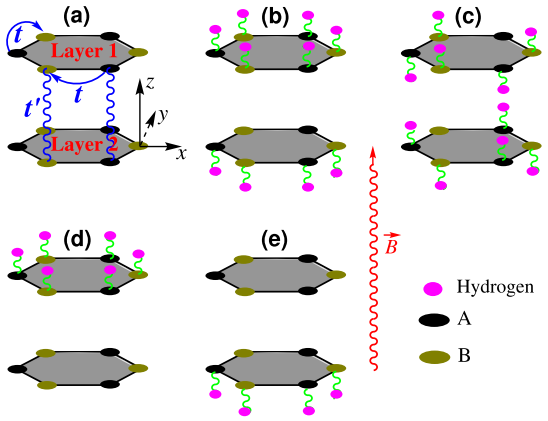

Fig. 1. (Color online.) Geometry of hydrogenated AA-stacked bilayer graphene for (a) pristine, (b) table-like, (c) chair-like, (d) r-table-like, and (e) r-chair-like case. The *intralayer* and *interlayer* hopping energies are labeled by t and t', respectively. The perpendicular magnetic field is also applied in the z-direction as $\vec{B}$.

the combined effects of magnetic field and impurity on H-BLG. In this paper, theoretical calculations are performed using the tight-binding Hamiltonian model and the Green's function approach. Also, the electron–impurity interaction effect between the host electrons of H-BLG and the external impurities is considered by means of the Born approximation and T-matrix method. The details will be shown later. We report the electronic phase transition and mid states stemming from various interactions. In other words, here we show that how one can control the electronic properties of H-BLG for future logic applications.

The paper is organized as follows. In Sec. 2, we describe the effective Hamiltonian model for H-BLG in the presence of the magnetic field in detail in which the special attention is paid to the way of hydrogenating. In Sec. 3, we introduce the Born approximation and T-matrix in order to find the interacting Green's functions. Then, we calculate DOS using the Green's function elements derived from the perturbed Hamiltonian. The results will be presented in Sec. 4 and to conclude, we summarize our remarkable findings in Sec. 5.

2. Model description

The intent of this section is to introduce the model addressing H-BLG lattice to allow for a systematic and routine assessment of electronic phase transition. To describe the dynamics of Dirac fermions in presence of magnetic field, the following tight-binding model Hamiltonian has been used [60]:

$$\hat{\mathcal{H}} = \sum_{i,j}\sum_{\sigma,\sigma'}\sum_{\alpha,\beta}\left[t_{ij\sigma'}^{\alpha\beta\sigma} + \epsilon_i^{\alpha\sigma}\delta_{\alpha\beta}\delta_{ij}\delta_{\sigma\sigma'}\right]\hat{c}_i^{\dagger\alpha\sigma}\hat{c}_j^{\beta\sigma'} + g\mu_B B/2\sum_{i,l}\left[\hat{a}_{li,\uparrow}^{\dagger}\hat{a}_{li,\downarrow} + \hat{b}_{li,\uparrow}^{\dagger}\hat{b}_{li,\downarrow} + \text{H.c.}\right], \tag{1}$$

wherein $t_{ij\sigma'}^{\alpha\beta\sigma}$ defines the hopping integral between an electron with spin σ from subsite α in the unit cell i to another electron with spin σ' from subsite β in the unit cell j. $\epsilon_i^{\alpha\sigma}$ is the on-site energy for an electron with spin σ from subsite α in the unit cell i. The hydrogen contribution with spin up is included in the on-site energy. Also, l is used for the layer index. In this work, five forms of hydrogenation are considered, namely pristine, table-like, chair-like, reduced table-like (r-table-like), and reduced chair-like (r-chair-like). Since our structure is considered as bilayer including four atoms per unit cell [A_1, B_1, A_2, and B_2] without hydrogenation, as illustrated in Fig. 1(a), by considering one H atom

for each C atom and spin degree of freedom, the Hamiltonian can be presented by a 10×10 matrix

$$\hat{\mathcal{H}}(\vec{k}) = \begin{pmatrix} \hat{\mathcal{H}}_{11}(\vec{k}) & \hat{\mathcal{H}}_{12}(\vec{k}) & \hat{\mathcal{H}}_{13}(\vec{k}) \\ \hat{\mathcal{H}}_{12}^{\dagger}(\vec{k}) & \hat{\mathcal{H}}_{22}(\vec{k}) & \hat{\mathcal{H}}_{23}(\vec{k}) \\ \hat{\mathcal{H}}_{13}^{\dagger}(\vec{k}) & \hat{\mathcal{H}}_{23}^{\dagger}(\vec{k}) & \hat{\mathcal{H}}_{33}(\vec{k}) \end{pmatrix}, \tag{2}$$

where the term $\hat{\mathcal{H}}_{11}(\vec{k})$ for C atoms in the first layer is given by

$$\begin{aligned} \hat{\mathcal{H}}_{11}(\vec{k}) &= \begin{pmatrix} \hat{\mathcal{H}}_{A_1\uparrow A_1\uparrow} & \hat{\mathcal{H}}_{A_1\uparrow A_1\downarrow} & \hat{\mathcal{H}}_{A_1\uparrow B_1\uparrow} & \hat{\mathcal{H}}_{A_1\uparrow B_1\downarrow} \\ \hat{\mathcal{H}}_{A_1\downarrow A_1\uparrow} & \hat{\mathcal{H}}_{A_1\downarrow A_1\downarrow} & \hat{\mathcal{H}}_{A_1\downarrow B_1\uparrow} & \hat{\mathcal{H}}_{A_1\downarrow B_1\downarrow} \\ \hat{\mathcal{H}}_{B_1\uparrow A_1\uparrow} & \hat{\mathcal{H}}_{B_1\uparrow A_1\downarrow} & \hat{\mathcal{H}}_{B_1\uparrow B_1\uparrow} & \hat{\mathcal{H}}_{B_1\uparrow B_1\downarrow} \\ \hat{\mathcal{H}}_{B_1\downarrow A_1\uparrow} & \hat{\mathcal{H}}_{B_1\downarrow A_1\downarrow} & \hat{\mathcal{H}}_{B_1\downarrow B_1\uparrow} & \hat{\mathcal{H}}_{B_1\downarrow B_1\downarrow} \end{pmatrix} \\ &= \begin{pmatrix} 0 & g\mu_B B/2 & f(\vec{k}) & 0 \\ g\mu_B B/2 & 0 & 0 & f(\vec{k}) \\ f^*(\vec{k}) & 0 & 0 & g\mu_B B/2 \\ 0 & f^*(\vec{k}) & g\mu_B B/2 & 0 \end{pmatrix}, \end{aligned} \tag{3}$$

in which the structure factor is defined as $f(\vec{k}) = t\Big(1 + exp\Big[+\mathrm{i}\vec{k}\cdot\vec{a}_1\Big] + exp\Big[+\mathrm{i}\vec{k}\cdot\vec{a}_2\Big]\Big)$ for $t \simeq 3$ eV and $\vec{a}_1 = a_0\big(\sqrt{3}\hat{e}_x + \hat{e}_y\big)/2$ and $\vec{a}_2 = a_0\left(\sqrt{3}\hat{e}_x - \hat{e}_y\right)/2$ with $a_0 \simeq 1.4$ Å. The term $\hat{\mathcal{H}}_{12}(\vec{k})$ for interlayer hopping between layers is also described by

$$\begin{aligned} \hat{\mathcal{H}}_{12}(\vec{k}) &= \begin{pmatrix} \hat{\mathcal{H}}_{A_1\uparrow A_2\uparrow} & \hat{\mathcal{H}}_{A_1\uparrow A_2\downarrow} & \hat{\mathcal{H}}_{A_1\uparrow B_2\uparrow} & \hat{\mathcal{H}}_{A_1\uparrow B_2\downarrow} \\ \hat{\mathcal{H}}_{A_1\downarrow A_2\uparrow} & \hat{\mathcal{H}}_{A_1\downarrow A_2\downarrow} & \hat{\mathcal{H}}_{A_1\downarrow B_2\uparrow} & \hat{\mathcal{H}}_{A_1\downarrow B_2\downarrow} \\ \hat{\mathcal{H}}_{B_1\uparrow A_2\uparrow} & \hat{\mathcal{H}}_{B_1\uparrow A_2\downarrow} & \hat{\mathcal{H}}_{B_1\uparrow B_2\uparrow} & \hat{\mathcal{H}}_{B_1\uparrow B_2\downarrow} \\ \hat{\mathcal{H}}_{B_1\downarrow A_2\uparrow} & \hat{\mathcal{H}}_{B_1\downarrow A_2\downarrow} & \hat{\mathcal{H}}_{B_1\downarrow B_2\uparrow} & \hat{\mathcal{H}}_{B_1\downarrow B_2\downarrow} \end{pmatrix} \\ &= \begin{pmatrix} t' & g\mu_B B/2 & 0 & 0 \\ g\mu_B B/2 & t' & 0 & 0 \\ 0 & 0 & t' & g\mu_B B/2 \\ 0 & 0 & g\mu_B B/2 & t' \end{pmatrix}, \end{aligned} \tag{4}$$

for $t' \simeq 0.2$ eV. All constant elements in this paper are taken from Refs. [61–63]. The term $g\mu_B B$ is energy corresponding to the applied external magnetic field which couples only to the electron spin, μ_B is the Bohr magneton, and g is the degeneracy number. On the other hand, $\hat{\mathcal{H}}_{22}(\vec{k}) = \hat{\mathcal{H}}_{11}(\vec{k})$. It is necessary to mention that the distance between two layers of bilayer graphene has been considered of 3.35 Å [64–66]. Also, the tabular form of $\hat{\mathcal{H}}_{13}(\vec{k})$ and $\hat{\mathcal{H}}_{23}(\vec{k})$ for hopping between H and C atoms are given by

$$\hat{\mathcal{H}}_{13}(\vec{k}) = \begin{pmatrix} \hat{\mathcal{H}}_{A_1\uparrow H_1\uparrow} & \hat{\mathcal{H}}_{A_1\uparrow H_2\uparrow} \\ \hat{\mathcal{H}}_{A_1\downarrow H_1\uparrow} & \hat{\mathcal{H}}_{A_1\downarrow H_2\uparrow} \\ \hat{\mathcal{H}}_{B_1\uparrow H_1\uparrow} & \hat{\mathcal{H}}_{B_1\uparrow H_2\uparrow} \\ \hat{\mathcal{H}}_{B_1\downarrow H_1\uparrow} & \hat{\mathcal{H}}_{B_1\downarrow H_2\uparrow} \end{pmatrix}, \tag{5a}$$

$$\hat{\mathcal{H}}_{23}(\vec{k}) = \begin{pmatrix} \hat{\mathcal{H}}_{A_2\uparrow H_1\uparrow} & \hat{\mathcal{H}}_{A_2\uparrow H_2\uparrow} \\ \hat{\mathcal{H}}_{A_2\downarrow H_1\uparrow} & \hat{\mathcal{H}}_{A_2\downarrow H_2\uparrow} \\ \hat{\mathcal{H}}_{B_2\uparrow H_1\uparrow} & \hat{\mathcal{H}}_{B_2\uparrow H_2\uparrow} \\ \hat{\mathcal{H}}_{B_2\downarrow H_1\uparrow} & \hat{\mathcal{H}}_{B_2\downarrow H_2\uparrow} \end{pmatrix}, \tag{5b}$$

where the elements of these two Hamiltonians depend strongly on the type of hydrogenation, as mentioned in Fig. 1. The values of these elements will be given later when analyzing the respective results. As for $\hat{\mathcal{H}}_{33}(\vec{k})$ between H atoms, we have

$$\hat{\mathcal{H}}_{33}(\vec{k}) = \begin{pmatrix} t_p & 0 \\ 0 & t_p \end{pmatrix}, \tag{6}$$

for $t_p = -2.4$ eV. In our calculations, we set all physical constants equal to unity. By using Eq. (2), the explicit form of Green's function matrix can be found by the following relation [67]

$$\hat{G}^{-1}(\vec{k}, \mathrm{i}\omega_n) = \mathrm{i}\omega_n \hat{I} - \hat{\mathcal{H}}(\vec{k}) \tag{7}$$

where $\mathrm{i}\omega_n \to \mathcal{E} + \mathrm{i}0^+$ refers to the fermionic Matsubara frequency [67] in the numerical calculation in which $0^+ = 5$ meV is a very small real number. The Green's function obtained in Eq. (7) is used to find DOS of the mentioned lattice. The details of calculations in terms of Green's function is presented in the following. DOS can be calculated by tracing over the imaginary part of diagonal Green's function elements as

$$\mathcal{D}_0(\mathcal{E}) = -\frac{1}{2\pi N_a N_c} \sum_{\vec{k}} \sum_{\mu=1}^{10} \mathrm{Im}\Big[G_0^{\mu\mu}(\vec{k}, \mathcal{E})\Big], \tag{8}$$

where μ describes a sub-site (A, B, and H) and 2 stands for the spin degree of freedom. N_a and N_c are the number of atoms in the unit cell and the number of unit cells, respectively. Furthermore, it should be mentioned that the sum over vector $\vec{k}$ is taken over the honeycomb reciprocal space, i.e. the first Brillouin zone (FBZ). The study of DOS in H-BLG in the presence of a magnetic field and impurity constitutes the main aim in this work. In the next section, the electron–impurity interaction effect will be discussed in detail. Furthermore, the perturbed DOS will be calculated using the interacting Green's function elements after considering the electron–impurity coupling.

3. Electron–impurity interaction

In this paper, we investigate the effects of *dilute* charged impurity on the electronic properties of H-BLG when doping *randomly*. The place of the doped impurity is not mattered within our formalism and we only have information on the concentration of the impurity and the scattering potential induced to the whole system. To this end, we use the Born approximation in the scattering theory and T-matrix [67]. In the Born approximation framework, the self-energy $\Sigma(\vec{p}, \mathcal{E})$ is a state-independent constant for electron–impurity interaction

$$\hat{\Sigma}(\vec{p}, \mathcal{E}) = n_i v_i \left[1 - \frac{v_i}{N_i} \sum_{\vec{k}\in FBZ} \hat{G}_0(\vec{k}, \mathcal{E})\right]^{-1}, \tag{9}$$

where N_i, n_i, v_i, and $\vec{p}$ are the number of impurity atoms per unit cell, the impurity concentration, impurity scattering potential, and the wave-vector induced by impurity to the host electrons, respectively. Through the Dyson equation, the perturbed configuration of Green's function reads [67]

$$\hat{G}(\vec{k},\mathcal{E}) = \hat{G}_0(\vec{k},\mathcal{E})\Big[1 - \hat{G}_0(\vec{k},\mathcal{E})\hat{\Sigma}(\vec{p},\mathcal{E})\Big]^{-1}. \tag{10}$$

Manifestly, the electronic *perturbed* DOS computes by mean of the imaginary part of the trace of the *interacting* Green's function matrix:

$$\mathcal{D}(\mathcal{E}) = \frac{-1}{2\pi N_a N_c}\sum_{\vec{k}}\sum_{\mu=1}^{10}\mathrm{Im}\Big[G_{\mu\mu}(\vec{k},\mathcal{E})\Big]. \tag{11}$$

In the next section, using the electronic disordered DOS-derived above, we examine the numerical results for electronic features of impurity-infected H-BLG subjected to a magnetic field. Although the Green's function matrix can be obtained analytically in our model, here we proceed with a numerical calculation.

4. Results and discussions

In this section, we intend to analyze the effect of charged impurity and the magnetic field on H-BLG with different hydrogenation configurations. It should be noted that henceforth, we use t as energy unit in numerical calculations; concomitantly all energies are measured in units of $1/t$. The section is divided into three parts. First, we will focus on building an intuitive understanding of the effective way of hydrogenation in our formalism. In other words, we need to know which kind of hydrogenation ways proposed in Fig. 1 gives rise to fascinating properties. This task requires the knowledge of DOS for each configuration, which will be presented in Fig. 2. Also, we will present the behavior of DOS in a fixed uniform magnetic field for the chosen configurations in Fig. 3 in order to see the difference between their behaviors in the absence and presence of magnetic field.

Second, we will study the chosen systems for a wide range of applied magnetic field in Figs. 4–6. In particular, we choose different values for the magnetic field, namely $g\mu_B B/t = 0, 0.2, 0.5$, and 0.8. These values have been chosen since $g\mu_B B > t$ gives the unstable lattice, while it is reasonable to have $g\mu_B B < t$ to conserve the stability of the system. Even though the main aim is finding the scattering effect between the magnetic field wave and the host electronic waves, we should take care of the stability of the system even theoretically.

Finally, in the third part, as a proof of principle for new electronic features of the combined effect of impurity and magnetic field, we consider a narrow energy depicted in Figs. 7–9. The chosen narrow energy is a consequence of the previous reports, which the most important alterations took place near the Fermi level. It is assumed that the systems before and after applying the magnetic field and impurity are in their optimized state. It is worthwhile to note that to observe new electronic properties such as electronic phase transition in H-BLG, we need to perform numerical calculations for momenta belonging to hexagonal FBZ with ranges $-2\pi/\sqrt{3}a_0 \le k_x \le +2\pi/\sqrt{3}a_0$ and $-4\pi/3a_0 \le k_y \le +4\pi/3a_0$. Furthermore, we set in all the calculations of DOS the Fermi level to zero.

Before entering into the details of the results, let us write the key points of DOS treatment in general. Electronic DOS gives us the information on the electronic state distribution of particles (electrons and holes) in an electronic system based on the respective places of states in valence and conduction band, i.e. with positive and negative energy, respectively. Indeed, it tells us how many states are located per electron volt (eV) in each energy band. Thereby, by using this, the degenerate states appear depending on the peaks in DOS curves. Note that the main differences between the degree of occupied and unoccupied energy levels are that in the more occupied levels the higher peaks in DOS emerge, whilst the fewer ones correspond to the unoccupied or less occupied states. In addition, we expect the zero and non-zero value

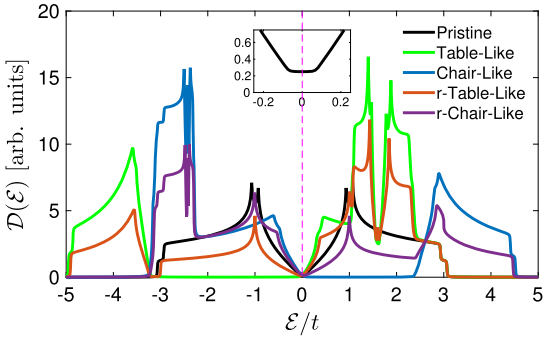

Fig. 2. (Color online.) The electronic DOS of pristine BLG and H-BLGs. The systems are in the absence of impurity and magnetic field in this figure. The Fermi level is set to zero (magenta vertical dashed line at $\mathcal{E}/t = 0$).

for DOS around the Fermi level for semiconductor/insulator and semimetal/metal devices because in the semiconductor/insulator materials there is no state in the vicinity of Fermi level, whereas there is overlapped states for the semimetal/metal ones [67,68]. One thing more about DOS refers to the conservation of the area under the curve. This point should be considered always. However, we do not compute the area under curves in the present work and it can be observed from the curves when shifting up/down and/or right/left. Accordingly, we restrict ourselves to this phase degeneration in our calculations to determine the electronic phase of the systems.

Now it is time to list the Hamiltonians $\hat{\mathcal{H}}_{13}(\vec{k})$ and $\hat{\mathcal{H}}_{23}(\vec{k})$ for $t_1 = t_2 = 5.72$ eV:

$$\hat{\mathcal{H}}_{13}^{\mathrm{TL}}(\vec{k}) = \begin{pmatrix} -t_1 & 0 \\ -g\mu_B B/2 & 0 \\ -t_1 & 0 \\ -g\mu_B B/2 & 0 \end{pmatrix}, \hat{\mathcal{H}}_{23}^{\mathrm{TL}}(\vec{k}) = \begin{pmatrix} 0 & t_2 \\ 0 & g\mu_B B/2 \\ 0 & t_2 \\ 0 & g\mu_B B/2 \end{pmatrix}, \tag{12a}$$

$$\hat{\mathcal{H}}_{13}^{\mathrm{CL}}(\vec{k}) = \begin{pmatrix} -t_1 & 0 \\ -g\mu_B B/2 & 0 \\ t_1 & 0 \\ g\mu_B B/2 & 0 \end{pmatrix}, \hat{\mathcal{H}}_{23}^{\mathrm{CL}}(\vec{k}) = \begin{pmatrix} 0 & t_2 \\ 0 & g\mu_B B/2 \\ 0 & -t_2 \\ 0 & -g\mu_B B/2 \end{pmatrix}, \tag{12b}$$

$$\hat{\mathcal{H}}_{13}^{\mathrm{rTL}}(\vec{k}) = \begin{pmatrix} 0 & 0 \\ 0 & 0 \\ 0 & 0 \\ 0 & 0 \end{pmatrix}, \hat{\mathcal{H}}_{23}^{\mathrm{rTL}}(\vec{k}) = \begin{pmatrix} 0 & t_2 \\ 0 & g\mu_B B/2 \\ 0 & t_2 \\ 0 & g\mu_B B/2 \end{pmatrix}, \tag{12c}$$

$$\hat{\mathcal{H}}_{13}^{\mathrm{rCL}}(\vec{k}) = \begin{pmatrix} 0 & 0 \\ 0 & 0 \\ 0 & 0 \\ 0 & 0 \end{pmatrix}, \hat{\mathcal{H}}_{23}^{\mathrm{rCL}}(\vec{k}) = \begin{pmatrix} 0 & t_2 \\ 0 & g\mu_B B/2 \\ 0 & -t_2 \\ 0 & -g\mu_B B/2 \end{pmatrix}. \tag{12d}$$

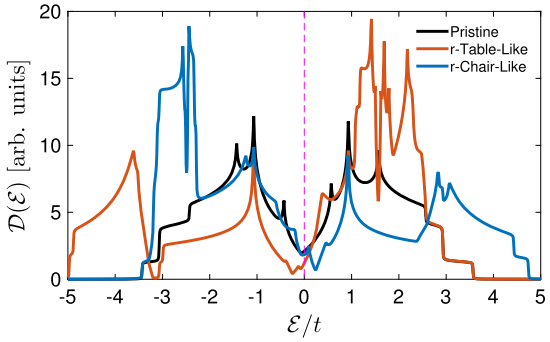

Fig. 3. (Color online.) The comparison between DOS of pristine BLG, rTL H-BLG, and rCL H-BLG subjected to a constant magnetic field $g\mu_B B/t = 0.5$ when the impurity atoms are absent.

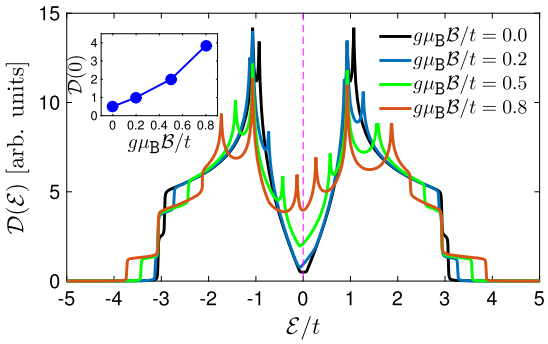

Fig. 4. (Color online.) The effect of magnetic field on the electronic DOS of pristine BLG when the impurity atoms are absent.

4.1. DOS of pristine BLG and H-BLGs with and without magnetic field

Let us start by investigating the electronic DOS as a function of normalized energy $\mathcal{E}/t$ from -5 eV to $+5$ eV in the absence of a magnetic field and impurity doping. In Fig. 2 DOS of pristine BLG, table-like H-BLG, chair-like H-BLG, r-table-like H-BLG, and r-chair-like H-BLG is illustrated, respectively, for $g\mu_B B/t = 0$, $n_i = 0\%$, and $v_i/t = 0$. In this figure, we have used Eq. (8), the *unperturbed* DOS for different electronic correlations between C and H atoms provided by the Green's function elements. Observe that the agreement of pristine result of DOS [the black color] with the results of Ref. [69] is excellent. This confirmation allows us to proceed for the hydrogenated versions of BLG, the other colors in the figure. It can be seen that DOS of pristine BLG exhibits two logarithmic spikes, so-called the van Hove singularities around $\mathcal{E}/t = \pm 1$, whereas more than two appears in the case of hydrogenated ones. The van Hove singularity describes the degenerate state in the electronic structure. Appearing more degenerate states are logical here due to the newly added states stemming from H atoms to the structure. On the one hand, two van Hove singularities which are main characters of BLG (it is one in the case of monolayer graphene) disappears when doping H atom on both layers, i.e. table-like and chair-like cases.

It is interesting to note that at the very beginning that the table-like and chair-like H-BLGs are *insulator* systems because of their wide band gap of $\simeq 2.2t$ and $\simeq 3.1t$ around the Fermi level, respectively. Also, one can see an electron–hole symmetry for this table- and chair-like H-BLGs at a fairly low-energy limit, as magnified in inset panel for the pristine BLG. On the other hand, the reduced versions of these H dopings to only one of the layers shows remarkable behaviors compared to the H doped on both layers. Surprisingly, the merger of hydrogenated one of the layers showcases the electronic DOS of monolayer graphene in the range of $-1.5 \leq \mathcal{E}/t \leq +1.5$. It means that in the case of r-table-like and r-chair-like H-BLGs, we deal with two almost gapless *semiconductor* systems. Generically, DOS at $-0.75 \leq \mathcal{E}/t \leq +0.75$ is symmetric in all cases, i.e. $\mathcal{D}(\mathcal{E}) = \mathcal{D}(-\mathcal{E})$. For these reasons, we are interested in two latter configurations much more than the former insulator ones. In what follows, a proper interpretation of our main outcomings is focused on pristine BLG, r-table-like (rTL) and r-chair-like (rCL) H-BLGs.

Now we turn to study the DOS of selected systems when a perpendicular magnetic field is present. We have numerically performed the same calculations by assuming that the contribution of both spin-up and spin-down are the same [due to the proposed model in Eq. (1)]. For this reason, we have focused on $\mathcal{D}(\mathcal{E}) = \left[\mathcal{D}^{\uparrow}(\mathcal{E}) + \mathcal{D}^{\downarrow}(\mathcal{E})\right]$ when dealing with the magnetic field throughout the paper. Additionally, we stress that the electronic DOS depends strongly on the strength of the magnetic field due to the magnetic field-dependent Hamiltonian in Eqs. (3) and (4). To see this point, in Fig. 3 we plot DOS for pristine BLG, rTL H-BLG, and rCL H-BLG lattices at $g\mu_B B/t = 0.5$. It is clear that DOS curves are changed as soon as the magnetic field is turned on. At first glance, one observes that the electron–hole symmetry is broken in pristine BLG [the black color] and two spikes split into three ones in both negative and positive energy sides. The new degenerate states corresponding to these new spikes in both sides originate from the Zeeman effect based on our proposed Hamiltonian in Eq. (1). This is valid for other two lattices as well, i.e. extra degenerate states appear compared to the cases without the magnetic field in Fig. 2.

Nevertheless, the most considerable point in this figure is that the electronic phase of the systems changes either for pristine BLG or rTL and rCL H-BLGs when $g\mu_B B/t = 0.5$. As $g\mu_B B/t$ moves away from zero, a semimetal-to-metal and gapless semiconductor-to-semimetal phase transition occurs for pristine BLG and rTL and rCL H-BLGs, respectively. The main reason of symmetry breaking and electronic phase transition can be understood from the charge distribution of the carriers in the system. Actually, the initial distribution of electronic waves is destroyed when involving with new perturbation wave (magnetic field). Further, one can expect that the area under curves is conserved after magnetic field because of the shifting up and right/left sides. The strong dependence of the electronic DOS on $g\mu_B B/t$ can be examined further in detail in the following.

4.2. DOS of pristine BLG, rTL H-BLG, and rCL H-BLG subjected only to the magnetic field

So far, we have been analyzing the unperturbed lattices and in short the magnetic field-induced ones. To infer whether the van Hove singularities and/or the electronic phase of the systems change with the magnetic field, throughout the following analysis in this subsection, we will not consider the impurity effects for all three lattices yet. Paying attention to the discussion of the magnetic field effects mentioned in the previous part on the electronic properties of chosen lattices [see Fig. 3], we show DOS of pristine BLG in Fig. 4. Here, we observe a similar treatment for DOS as in the case $g\mu_B B/t = 0.5$, i.e. the rise in DOS at $\mathcal{E}/t = 0$ beside the splitting the pronounced peaks at $\mathcal{E}/t = \pm 1$. By increasing the magnetic field the broadening of van Hove singularities is increased and the electron–hole symmetry between the valence and conduction bands is no longer visible, and instead we can see that the intensity of DOS around the Fermi level $\mathcal{D}(0)$ increases [see the inset panel], leading to a semimetal-to-metal electronic phase transition. These new features stem from magnetic field-induced states, which is again due to the Zeeman splitting effects. As we increase the strength of the magnetic field, the height of the peaks decreases and DOS moves toward the higher negative and positive energies. This comes from the general rule of conservation of the

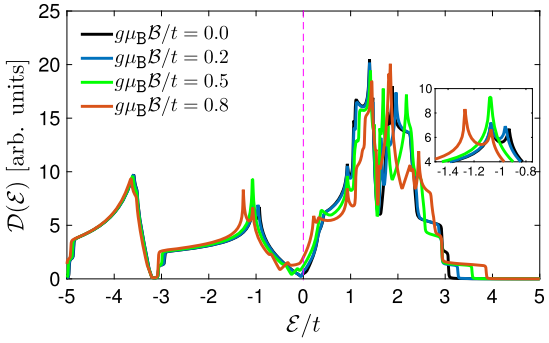

Fig. 5. (Color online.) The calculated DOS of r-table-like H-BLG in the absence (absence) of impurity doping (magnetic field).

area under DOS. In particular, physically point of view, the probability density increases at higher energies when the magnetic field is present, which can be understood better by the spectral function quantity (out of the scope of the present paper).

As discussed before, when turning on the Zeeman magnetic field we will observe electronic phase transition from gapless semiconductor to semimetal which, in turn, generate phase as new scattering process is introduced. This can be regarded as a band overlapping process around the Fermi level. This strongly motivates us to calculate further the effect of magnetic field (less and more than $g\mu_B B/t = 0.5$) on DOS of rTL H-BLG in Fig. 5. We show in Fig. 5 the electronic DOS of rTL H-BLG corresponding to the magnetic field-induced states belonging to FBZ for magnetic field strengths $g\mu_B B/t = 0, 0.02, 0.5$, and 0.8. As can be seen from the figure, the role of the coupling between external magnetic field and electron spins is to create overlapped valence and conduction bands in the vicinity of Fermi level $\mathcal{E}/t = 0$, and adding new degenerate states in the energy range -5 eV and $+5$ eV. Comparing the plots for pristine BLG and rTL H-BLG, we first notice that, in the absence of impurity doping, DOS peaks in rTL H-BLG do not alter effectively or not depend strongly on the magnetic field strength. However, quite the contrary, in the pristine BLG, there is a critical value for the magnetic field, in which, before and after that, DOS has different behaviors around $\mathcal{E}/t = -1$. For instance, see the inset panel of Fig. 5, two van Hove singularities can be observed before and after $g\mu_B B/t = 0.5$, whereas there is only one peak at $g\mu_B B/t = 0.5$. This is not the case in pristine BLG [see Fig. 4]. One thing more is the effect of magnetic field on both valence and conduction bands. In the case of pristine BLG, both sides are affected significantly, whilst for rTL H-BLG, only the conduction band (the positive side of the energy axis) is affected when increasing the magnetic field.

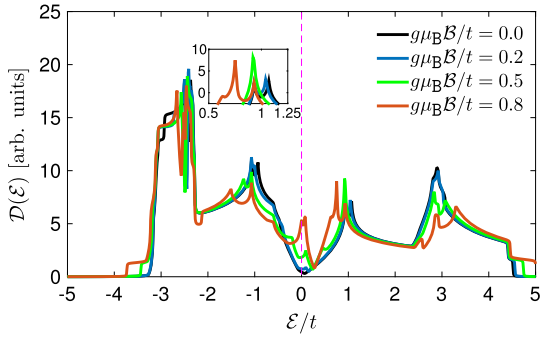

Fig. 6. (Color online.) The numerical results for DOS of r-chair-like H-BLG subjected to the magnetic field without electron–impurity interaction effect.

Results of DOS of rCL H-BLG are shown in Fig. 6 as well. As expected, the electronic DOS around $\mathcal{E}/t = 0$ increases with increasing Zeeman magnetic field. All information regarding the splitting effects and electronic phase transition valid again here. There is a gapless semiconductor-to-semimetal phase transition at $\mathcal{E}/t = 0$ when the magnetic field is increased. Note that the formation of overlapped states of valence and conduction bands are completely different as a function of energy $\mathcal{E}/t$, indicating that both energy sides are affected by the magnetic field. Apart from these, still, the critical magnetic field $g\mu_B B/t = 0.5$ is observed here as before and after that, the number of van Hove singularities around $\mathcal{E}/t = +1$ are two, while it is only one at $g\mu_B B/t = 0.5$.

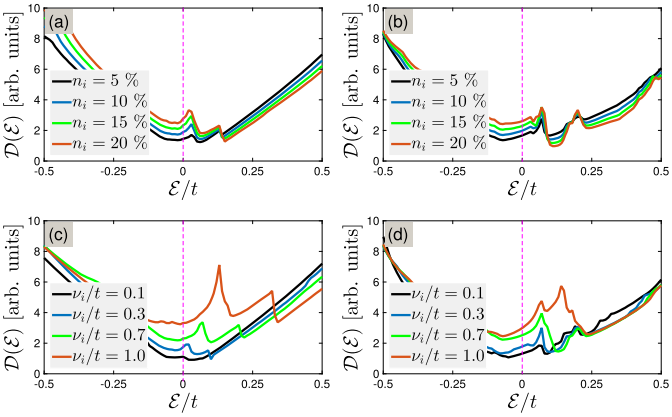

Fig. 7. (Color online.) The effect of charged impurity on the electronic DOS of pristine H-BLG for (a) different n_i without magnetic field, (b) different n_i with $g\mu_B B/t = 0.4$, (c) different ν_i/t without the external magnetic field, and (d) different ν_i/t with $g\mu_B B/t = 0.4$.

4.3. Impurity-infected DOS of pristine BLG, rTL H-BLG, and rCL H-BLG with and without the magnetic field

So far, we have not considered the impurity doping effects in all lattices and only we dealt with the magnetic field. In what follows, the *dilute* charged impurity will be considered in the absence and presence of the magnetic field in order to see how the electronic phase of the pristine BLG, rTL H-BLG, and rCL H-BLG systems will be enhanced. After establishing the effect of a *magnetic* perturbation on our systems it is worthwhile to concisely cover some of the key features of the *electronic* perturbation effects before we end the paper. Since the most important features in previous plots happened to the low-energy limit of DOS, we restrict ourselves to the energy range from $-1/2$ to $+1/2$, not the whole range of energy considered before, as shown in panels (a)–(d) of Figs. 7–9.

Let us first explain two scenarios considered in this part. In all cases systems are doped with *the same* impurities (different n_i and fixed ν_i/t) and *different* impurities (different ν_i/t and fixed n_i) in the absence and presence of magnetic field. In Figs. 7–9, panels (a), (b), (c), and (d) correspond to the different n_i without magnetic field, different n_i with magnetic field, different ν_i/t without magnetic field, and different ν_i/t with magnetic field, respectively. When fixing n_i, ν_i/t, and $g\mu_B B/t$ we use values 10%, 0.5, and 0.4, respectively.

The electronic DOS of charged impurity-infected pristine BLG is shown in Fig. 7. In Fig. 7(a) although DOS without magnetic field increases within the energy range of $\mathcal{E}/t = -1/2$ to $\mathcal{E}/t = +1/8$ with increasing impurity concentration n_i, it decreases slightly for the case of $\mathcal{E}/t > +1/8$, leading to the semimetal-to-metal electronic phase transition overall. In Fig. 7(b) when impurity-infected pristine BLG is subjected to a magnetic field $g\mu_B B/t = 0.4$, two different behaviors besides the semimetal-to-metal phase transition occur. From $\mathcal{E}/t = -1/2$ to $\mathcal{E}/t = +1/16$, DOS increases with n_i albeit mostly close to the Fermi level and from $\mathcal{E}/t > 1/16$ DOS decreases with n_i slightly. This means that the competition be-

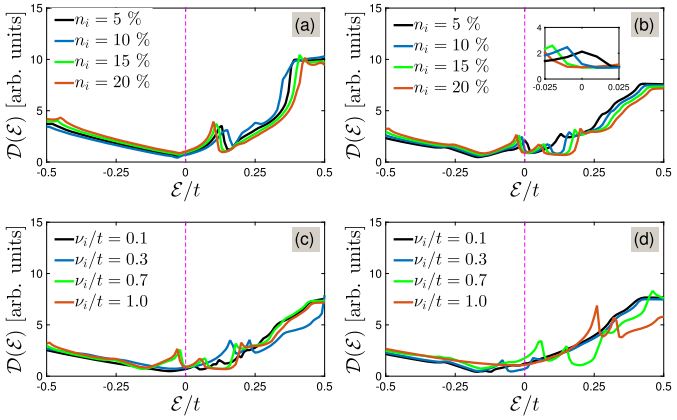

Fig. 8. (Color online.) The charged impurity-dependent electronic DOS of r-table-like H-BLG for (a) different n_i without magnetic field, (b) different n_i with $g\mu_B B/t = 0.4$, (c) different ν_i/t without the external magnetic field, and (d) different ν_i/t with $g\mu_B B/t = 0.4$.

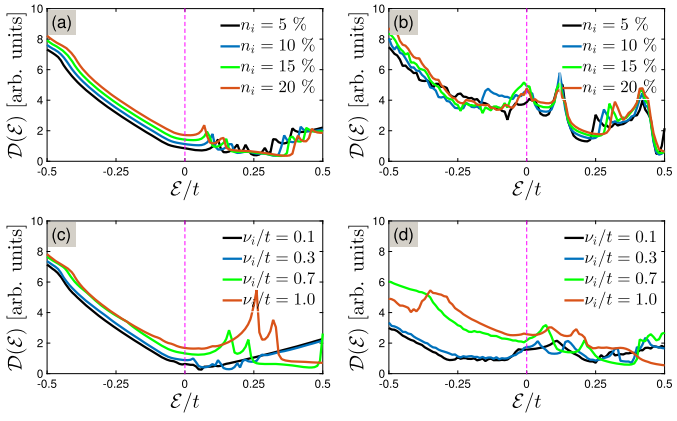

Fig. 9. (Color online.) The charged impurity-dependent electronic DOS of r-table-like H-BLG for (a) different n_i without magnetic field, (b) different n_i with $g\mu_B B/t = 0.4$, (c) different ν_i/t without the external magnetic field, and (d) different ν_i/t with $g\mu_B B/t = 0.4$.

tween the magnetic perturbation ($g\mu_B B/t = 0.4$) and electronic one ($n_i \in [0\%–20\%]$) affects the scattering process of carriers. For this reason, finding the proper energy level for their new situation and distribution differs than before. To cover the second scenario we have investigated ν_i/t-dependent DOS as a function of $\mathcal{E}/t$ in the presence of perturbations. In Fig. 7(c), significant changes can be observed for different ν_i/t. The electronic wave distribution of carriers alters more effectively than the case of n_i in panel (a). This big difference stems from the basic knowledge of this scenario. Different ν_i/t refers to differently doped impurities which obviously affects the scattering rate of carriers much more than the same ones. When the magnetic field is present, one can claim that the difference is not considerable and the system shows almost the same treatment, as presented in Fig. 7(d).

To characterize the mentioned effects on the hydrogenated versions of BLG, i.e. rTL and rCL H-BLGs, we now examine the electronic density of the corresponding states to the different configurations of impurity doping in the presence and absence of magnetic field. In Fig. 8 we plot the impurity-infected electronic DOS summed over the whole FBZ of rTL H-BLG without (left panels) and with (right panels) the Zeeman magnetic field. Interestingly, while the electronic DOS in the absence of magnetic field appears insensitive to the impurity concentration n_i [see Fig. 8(a)], it depends on how the impurity interacts with the magnetic field $g\mu_B B/t = 0.4$, as shown in Fig. 8(b). In other words, one can see that a gapless semiconductor to the gapped (p-doped) semiconductor phase transition occurs when the magnetic field is present in rTL H-BLG under the same impurity atoms doping process. On the other hand, this is not the case with different impurity atoms doping. In Fig. 8(c), in spite to the case of panel (a), DOS changes significantly with ν_i/t, resulting in a gapless semiconductor to the gapped (p-doped) semiconductor electronic phase transition again. However, the coexistence of impurity scattering potential and the magnetic field potential in panel (d) does not provide a remarkable alteration, and eventually no phase transition observes. Of course, new degenerate states (small peaks at $\mathcal{E}/t > 0$) are observed due to overlapped bands mentioned originating from the competition between ν_i/t and $g\mu_B B/t$.

To finish, let us briefly discuss the key findings of the electronic disordered DOS of rCL H-BLG observed when turning on and off the magnetic field [see Fig. 9]. As was mentioned before, for the case of different n_i and fixed ν_i/t corresponding to the same impurity atoms, the upper panels [(a) and (b)] are plotted, while the lower panels [(c) and (d)] refer to the different impurity atoms, i.e. different ν_i/t and ascertained n_i. Similar to the case of pristine BLG and rTL H-BLG, new behaviors for states close to the low-energy limit are observed. This implies that the new electronic phases are appeared to confirm our claim about the new features occurring in the presence of both impurity and magnetic field. In Fig. 9(a) we display the numerical data for DOS with different n_i without magnetic field as a function of $\mathcal{E}/t$ in order to compare them with previous lattices. Again, DOS increases with n_i up to an ascertained $\mathcal{E}/t$ for each n_i and afterward approaches the p-doped semiconductor phase due to the appeared band gap in the positive energy side. As for panel (b) in the presence of the magnetic field $g\mu_B B/t = 0.4$, there is no special trend and a phase transition from gapless semiconductor to the metal can be observed. On the other hand, the results for different ν_i/t and fixed $n_i = 10\%$ in panel (c) show that in strong scattering potentials the metal phase prevails even if the system is subjected to the $g\mu_B B/t = 0.4$ [see panel (d)], as one can expect for a system with scattered carriers.

5. Conclusions

We have studied the emergence of new states and different electronic phases in the pristine and hydrogenated bilayer graphene, taking into account the electron–impurity interaction and magnetic field effects. We have employed the tight-binding Hamiltonian model, the Born approximation, and the Green's function method to calculate the perturbed electronic DOS in these systems. We have demonstrated that different types of impurity and also the hydrogenation configuration lead to different phase transitions stemming from the charge distribution of carriers. For the case of without magnetic field and impurity, the semimetallic and gapless semiconducting phases are observed corresponding to the pristine and hydrogenated bilayer graphene, respectively. For the case of only the magnetic field, the electronic DOS tend to increase at low-energy limit, leading to the semimetal-to-metal phase transition, while a gapless semiconductor-to-semimetal occurs for hydrogenated ones. As further plans, we found that the phase of the pristine system only changes with impurity. For the combined effect of magnetic field and the charged impurity, we provide the phase back transitions. The impact of these factors in functionalized bilayer low-dimensional systems render a promising way to improve the electro-optical properties in the future logic devices.

Acknowledgements

M. Y. thanks Masoumeh Davoudiniya for gathering data in a private supercomputer. This research is funded by Vietnam National

Foundation for Science and Technology Development (NAFOSTED) under grant number 103.01-2017.361.

References

[1] Y. Zhang, Z. Jiang, J.P. Small, M.S. Purewal, Y.-W. Tan, M. Fazlollahi, J.D. Chudow, J.A. Jaszczak, H.L. Stormer, P. Kim, Phys. Rev. Lett. 96 (2006) 136806.
[2] K.S. Novoselov, A.K. Geim, S.V. Morozov, D. Jiang, Y. Zhang, S.V. Dubonos, I.V. Grigorieva, A.A. Firsov, Science 306 (2004) 666.
[3] C. Berger, et al., Science 312 (2006) 1191.
[4] A.H.C. Neto, F. Guinea, N.M.R. Peres, K.S. Novoselov, A.K. Geim, Rev. Mod. Phys. 81 (2009) 109.
[5] F. Xia, D.B. Farmer, T.-m. Lin, P. Avouris, Nano Lett. 10 (2010) 715.
[6] Y. Zhang, et al., Nature 459 (2009) 820.
[7] E.V. Castro, et al., Phys. Rev. Lett. 99 (2007) 216802.
[8] G. Gui, J. Li, J. Zhong, Phys. Rev. B 78 (2008) 075435.
[9] L. Sun, Q. Li, H. Ren, H. Su, Q.W. Shi, J. Yang, J. Chem. Phys. 129 (2008) 074704.
[10] G. Giovannetti, P.A. Khomyakov, G. Brocks, P.J. Kelly, J. van den Brink, Phys. Rev. B 76 (2007) 073103.
[11] X.F. Chen, J.S. Lian, Q. Jiang, Phys. Rev. B 86 (2013) 125437.
[12] Q.Q. Dai, Y. Zhu, Q. Jiang, Q.Q. Dai, Y. Zhu, Q. Jiang, J. Phys. Chem. C 117 (9) (2013) 4791.
[13] Q.Q. Dai, Y.F. Zhu, Q. Jiang, Phys. Chem. Chem. Phys. 16 (2014) 10607.
[14] L. Li, et al., ACS Nano 5 (2011) 2601.
[15] Y. Zhang, Y.V. Kartashov, F. Li, Zh. Zhang, Y. Zhang, M.R. Belić, M. Xiao, ACS Photonics 4 (9) (2017) 2250.
[16] Y. Zhang, Zh. Wu, M.R. Belić, H. Zheng, Zh. Wang, M. Xiao, Y. Zhang, Laser Photonics Rev. 9 (2015) 331.
[17] Y. Zhang, Zh. Wang, Zh. Nie, C. Li, H. Chen, K. Lu, M. Xiao, Phys. Rev. Lett. 106 (2011) 093904.
[18] Y. Zhang, D. Zhang, Zh. Zhang, C. Li, Y. Zhang, F. Li, M.R. Belić, M. Xiao, Optica 4 (2017) 571.
[19] D.C. Elias, et al., Science 323 (2009) 610.
[20] J. Zhou, Q. Wang, Q. Sun, X.S. Chen, Y. Kawazoe, P. Jena, Nano Lett. 9 (2009) 3867.
[21] D. Haberer, et al., Nano Lett. 10 (2010) 3360.
[22] R. Balog, et al., Nat. Mater. 9 (2010) 315.
[23] M.V. Ulybyshev, M.I. Katsnelson, Phys. Rev. Lett. 114 (2015) 246801.
[24] C. Lin, Y. Feng, Y. Xiao, M. Drr, X. Huang, X. Xu, R. Zhao, E. Wang, X.-Z. Li, Z. Hu, Nano Lett. 15 (2015) 903.
[25] K.M. McCreary, A.G. Swartz, W. Han, J. Fabian, R.K. Kawakami, Phys. Rev. Lett. 109 (2012) 186604.
[26] R.R. Nair, M. Sepioni, I.-L. Tsai, O. Lehtinen, J. Keinonen, A.V. Krasheninnikov, T. Thomson, A.K. Geim, I.V. Grigorieva, Nat. Phys. 8 (2012) 199.
[27] Y.F. Li, Z. Zhou, P.W. Shen, Z.F. Chen, J. Phys. Chem. C 113 (2009) 15043.
[28] F. Yndurain, Phys. Rev. B 90 (2014) 245420.
[29] D.W. Boukhvalov, M.I. Katsnelson, A.I. Lichtenstein, Phys. Rev. B 77 (2008) 035427.
[30] J.O. Sofo, A.S. Chaudhari, G.D. Barber, Phys. Rev. B 75 (2007) 153401.
[31] S. Lebègue, M. Klintenberg, O. Eriksson, M.I. Katsnelson, Phys. Rev. B 79 (2009) 245117.
[32] N. Lu, Z. Li, J. Yang, J. Phys. Chem. C 113 (2009) 16741.
[33] S.M. Ryu, et al., Nano Lett. 8 (2008) 4597.
[34] S.-M. Choi, S.-H. Jhi, Y.-W. Son, Nano Lett. 10 (2010) 3486.
[35] D.K. Samarakonn, X.-Q. Wang, ACS Nano 4 (2010) 4126.
[36] M.L. Ng, et al., J. Phys. Chem. C 114 (2010) 18559.
[37] J. Coraux, et al., New J. Phys. 11 (2009) 023006.
[38] H. Min, B. Sahu, S.K. Banerjee, A.H. MacDonald, Phys. Rev. B 75 (2007) 155115.
[39] W. Choi, I. Lahiri, R. Seelaboyina, Y.S. Kang, Crit. Rev. Solid State Mater. Sci. 35 (2010) 52.
[40] H. Min, A.H. MacDonald, Phys. Rev. B 77 (2008) 155416.
[41] Z. Luo, T. Yu, K. Kim, Z. Ni, Y. You, S. Lim, Z. Shen, S. Wang, J. Lin, ACS Nano 3 (2009) 1781.
[42] M. Moaied, J.V. Alvarez, J.J. Palacios, Phys. Rev. B 90 (2014) 115441.
[43] A. Guttler, T. Zecho, J. Kuppers, Surf. Sci. 570 (2004) 218.
[44] P. Sessi, J.R. Guest, M. Bode, N.P. Guisinger, Nano Lett. 9 (2009) 4343.
[45] M. Yang, A. Nurbawono, C. Zhang, Y.P. Feng, Appl. Phys. Lett. 96 (2010) 193115.
[46] M. Killi, S. Wu, A. Paramekanti, Phys. Rev. Lett. 107 (2011) 086801.
[47] J.M.B. Lopes dos Santos, N.M.R. Peres, A.H. Castro Neto, Phys. Rev. Lett. 99 (2007) 256802.
[48] K.S. Kim, et al., Nat. Mater. 12 (2013) 887.
[49] A. Luican, et al., Phys. Rev. Lett. 106 (2011) 126802.
[50] E. McCann, Phys. Rev. B 74 (2006) 161403.
[51] B.V. Duppen, F.M. Peeters, Phys. Rev. B 87 (2013) 205427.
[52] A. Jellal, I. Redouani, H. Bahlouli, Physica E 72 (2015) 149.
[53] H.D. Bui, M. Yarmohammadi, Solid State Commun. 280 (2018) 39.
[54] H.D. Bui, M. Yarmohammadi, Phys. Lett. A 382 (2018) 1885.
[55] M. Buscema, D.J. Groenendijk, S.I. Blanter, G.A. Steele, H.S.J. van der Zant, A. Castellanos-Gomez, Nano Lett. 14 (2014) 3347.
[56] H. Liu, A.T. Neal, Z. Zhu, Z. Luo, X.F. Xu, D. Tomanek, P.D. Ye, ACS Nano 8 (2014) 4033.
[57] G. Kim, A. Jang, H.Y. Jeong, Z. Lee, D.J. Kang, H.S. Shin, Nano Lett. 13 (2013) 1834.
[58] V. Georgakilas, et al., Chem. Rev. 112 (2012) 6156.
[59] C. Zhai, X. Dai, W. Li, Y. Ma, T. Wang, Y. Tang, Superlattices Microstruct. 101 (49) (2017).
[60] A.W. Harrison, Structure and the Properties of Solids, Dover, New York, 1989.
[61] R. Saito, G. Dresselhaus, M.S. Dresselhaus, Physical Properties of Carbon Nanotubes, Imperial College Press, London, 1998.
[62] V. Zolyomi, J.R. Wallbank, V.I. Falko, 2D Mater. 1 (2014) 011005.
[63] R. Grassi, T. Low, M. Lundstrom, Nano Lett. 11 (2011) 4574.
[64] J. Slawinska, I. Zasada, Z. Klusek, Phys. Rev. B 81 (2010) 155433.
[65] W. Zan, W. Geng, H. Liu, X. Yao, J. Alloys Compd. 666 (2016) 204.
[66] R.M. Ribeiro, N.M.R. Peres, Phys. Rev. B 83 (2011) 235312.
[67] G.D. Mahan, Many Particle Physics, Plenum Press, New York, 1993.
[68] C. Kittle, Introduction to Solid State Physics, eighth ed., Wiley, New York, 2004.
[69] C.J. Tabert, E.J. Nicol, Phys. Rev. B 86 (2012) 075439.